Molecular Dynamic Characteristic Temperatures for Predicting Metallic Glass Forming Ability

Lane E. Schultz^a, Benjamin Afflerbach^a, Izabela Szlufarska^a, and Dane Morgan^a

^aUniversity of Wisconsin-Madison, 1500 engineering Drive, Madison, WI 53706, USA

September 27, 2021

Abstract

We explore the use of characteristic temperatures derived from molecular dynamics to predict aspects of metallic Glass Forming Ability (GFA). Temperatures derived from cooling curves of self-diffusion, viscosity, and energy were used as features for machine learning models of GFA. Multiple target and model combinations with these features were explored. First, we use the logarithm of critical casting thickness, $log_{10}(D_{max})$, as the target and trained regression models on 21 compositions. Application of 3-fold cross-validation on the $21 \log_{10}(D_{max})$ alloys showed only weak correlation between the model predictions and the target values. Second, the GFA of alloys were quantified by melt-spinning or suction casting amorphization behavior, with allows that showed crystalline phases after synthesis classified as Poor GFA and those with pure amorphous phases as Good GFA. Binary GFA classification was then modeled using decision tree-based methods (random forest and gradient boosting models) and were assessed with nested-cross validation. The maximum F1 score for the precision-recall with Good Glass Forming Ability as the positive class was 0.82 ± 0.01 for the best model type. We also compared using simple functions of characteristic temperatures as features in place of the temperatures themselves and found no statistically significant difference in predictive abilities. Although the predictive ability of the models developed here are modest, this work demonstrates clearly that one can use molecular dynamics simulations and machine learning to predict metal glass forming ability.

Keywords: Metallic glasses, Characteristic temperatures, Machine learning, Glass forming ability, Critical casting diameter

1 Introduction

Determining metal alloy compositions that have good glass forming ability (GFA), and in particular that yield bulk metallic glasses, has been a grand challenge in metallic glass research for decades. Many previous attempts to predict GFA for metals have made use of some function of the temperatures characterizing important aspects of the melt behavior, sometimes called characteristic temperatures. The characteristic temperatures most used for this purpose are the glass transition (T_g) , the onset of crystallization (T_x) , and liquidus (T_l) temperatures. For example, the reduced glass transition temperature, $T_{rg} = T_g/T_l$, is one of the earliest and most iconic GFA indicator [1]. A very successful model for GFA predicts the critical cooling rate, R_c , as a linear function of $\omega = T_g/T_x - 2T_g/(T_g + T_l)$. When fit to 53 metallic glasses, a linear function between ω and R_c had an R^2 of 0.93 [2]. T_{rg} and ω are just two of over 20 functions

of T_g , T_x , and T_l that have been proposed to quantify GFA [3, 4]. Although successful models have only been shown for a small number of alloys, there are clear indications that insights into GFA can be given by characteristic temperatures.

Another GFA indicator, in this case from the melt, is the liquid fragility, m, which is measured by finding the slope of viscosity as a function of temperature near T_g for an alloy. Glasses with higher viscosities when approaching T_g are said to be strong (low m) and are thought to suppress the kinetics for crystallization. Conversely, glasses that experience low viscosities upon cooling are said to be fragile [5, 6]. It was shown that a linear combination of T_{rg} and m fit to $log_{10}(D_{max}^2)$ for 42 glassy alloys had an outstanding R^2 score of 0.980 [7]. Here, D_{max} is the critical casting diameter. Hence, D_{max} can be written as a relatively simple function of T_g , T_l , and m. Although m is not strictly a characteristic temperature it is similar in spirit as it represents the temperature dependent physics of the melt, and it can be related to a characteristic temperature as discussed later.

Quantitative relationships between the most important and intrinsic measure of GFA, specifically R_c and D_{max} , and characteristic temperatures (or closely related melt properties) can be established. However, the aforementioned relationships have limited utility for new material discovery because a glass must be synthesized to obtain the features T_g , T_x , and m. T_l must also be obtained, although this temperature can be measured without making a glass and is often accessible through thermodynamic modeling without actual synthesis. An exciting design opportunity would be realized if we could access T_g , T_x , T_l , and m from molecular simulations, as this would allow the above correlations to be used for computational prediction of GFA. It is this opportunity that motivate the present work.

 T_l can be predicted from molecular simulations quite accurately [8–10] and is often available from thermodynamic models fit to experiments for relevant alloys, so we will not focus further on this quantity and simply take it from experiments or online phase diagrams when available for the rest of the present study. T_g , T_x , and m are all in theory accessible to molecular simulations but have major practical challenges. T_g from molecular dynamic (MD) studies are strongly impacted by the very fast cooling rates necessitated by the short time scales accessible to MD. The MD values of T_g tend to be higher than experimental values due to heating/cooling rate differences and adopted methodology [11, 12]. See Ref. [11] for a comparison of experimental and MD approaches for finding T_g . Finally, another set of limitations are imposed by T_x calculation. As seen in Ref. [13], the crystallization kinetics in MD for a single composition varies by system size and annealing temperatures explored. The aforementioned indicates that mimicking an experimental T_x value from differential scanning calorimetry (DSC) would pose many challenges in choices of system sizes, cooling rates to attain a glass, heating rates, and the starting temperature to heat a material. m is also difficult to practically calculate from MD as it requires determining viscosity as a function of temperature near T_g , which is impractical due to the slow kinetics near T_q . Equations with reliable extrapolation to low temperature viscosities have their own set of challenges for finding their fitting parameters with MD [14, 15]. Due to these obstacles, direct MD of some experimental characteristic temperatures is currently impractical.

Nevertheless, MD accessible quantities that approximate or correlate with some of the previously defined material properties exist. For example, Kelton et al. have shown correlations between m and the ratio between T_g and a temperature where a set of compositions cross a set viscosity value, T^* [16, 17]. They further showed that T_g can be captured as a function of T^* , and the crossover from Arrhenius behavior temperature, T_A^* [18]. Specifically, a fit between T_A^*/T_g and T_g/T^* had an T_g of 0.96 [17]. The results from Kelton et al. and in Ref. [7] together imply that D_{max} should be a function of T_g , T^* , T_A^* , and T_l .

Other alloy characteristic temperatures are MD acquirable and included in this study. We choose to examine self-diffusion derived temperatures because trends between self-diffusion, viscosity, and relaxation times with respect to temperature show strong relationships, as seen in Ref. [19]. Parallel to the way T^* and T_A^* are defined for viscosity, we define T^{\prime} and T_A^{\prime} as the temperatures where diffusivity reaches a critical value and where diffusivity deviates from an Arrhenius trend, respectively. We can find an approximate T_g by direct high-rate cooling, which we call T_{gm} . Approximate T_g values can also be estimated by fitting to high-temperature kinetic properties with a simple Vogel-Fulcher-Tamman (VFT) form and extrapolating. We use this approach to define T_g^* as the temperature where extrapolated viscosity reaches 10^{12} $Pa \cdot s$ [20] and T_g^{\prime} as the temperature where extrapolated self-diffusion values reach $10^{-12} \, \text{Å}^2/ps$ (which is the method used to define T_g in Ref. [21]).

We argue and show that GFA insights could be gained from the MD characteristic temperatures of T_{gm} , T_g^* , T_A^* , T_g^* , T_A^* , T_g^{\prime} , T_A^{\prime} , and T_l . We use both regression and classification machine learning (ML) models to quantify the ability of models to learn GFA from MD characteristic temperatures. Although the examined data sets were small, preliminary results suggest that MD quantification of GFA is possible.

2 Methods

2.1 Molecular Dynamics

All MD simulations were performed with the LAMMPS package [22]. The time step was set to 1 fs. Periodic boundary conditions were applied along all directions. Finnis-Sinclair (FS) and embedded-atom model (EAM) potentials were used to simulate alloys of interest [23–29]. The starting MD supercell structures were built with a repeating simple cubic unit cell with 1,000 atoms. The element type for each atom was assigned randomly to match compositions of interest. An isothermal hold at 2,000 K was run for 100 ps under the NPT ensemble and was used as the initial trajectory for melt quench simulations. In the NPT ensemble, N is the number of atoms, P is the pressure, and T is the temperature and are all held constant.

Continuing from the starting structures, isothermal holds were constructed by dropping 100 K from the preceding hold. Each of the holds were ran for 10 ps which gave a cooling rate of $10^{13} K/s$. The final temperature probed was 100 K. For each of the isothermal holds from the melt-quench simulation, the final trajectory was run for an additional 10 ns under the NVT ensemble. In the NVT ensemble, N is the number of atoms, V is the system volume, and T is the temperature and are all held constant. For self-diffusion and viscosity, the reference time for calculations was at the beginning of the 10 ns isothermal hold. Mean squared displacement (MSD) for self-diffusion, viscosity, and averaged thermodynamic data were attained from the last 2 ns of the 10 ns isothermal hold. Each composition was run 2 times with different starting atomic positions for averaging characteristic temperature measurements to reduce uncertainty.

2.2 Kinetic Properties

Self-diffusion for each isothermal hold from quench runs was calculated through the long-time limit of MSD with Equation 1 [30]. In Equation 1, D is the self-diffusion, N is the total number of atoms, t is the time, and t is the position of an atom t. If the average mean squared displacement of atoms is less than 1 Å², we assumed that the atoms cannot be reliably identified as diffusing rather than just vibrating in place and the associated self-diffusion value was excluded from all

future analysis and our VFT fits to data.

$$D = \lim_{t \to \infty} \frac{1}{6Nt} \left\langle \sum_{i=1}^{N} \left[r_i(t) - r_i(t=0) \right]^2 \right\rangle$$
 (1)

The Green-Kubo formalism was used to calculate viscosity (Equation 2) in an equilibrated system by integrating the autocorrelation of the pressure tensor off-diagonals [19, 30–32]. In Equation 2, k_B is the Boltzmann's constant, T is the temperature, V is the system volume, t_0 is the starting time, t is a time value, and $P_{ij} \in \{P_{xy}, P_{xz}, P_{yz}\}$ are the elements of the pressure tensor. For a three-dimensional simulation, the integral of the autocorrelation of P_{xy} , P_{xz} , and P_{yz} can be averaged together due to their symmetry equivalence in the liquid state.

$$\eta = \frac{V}{k_B T} \int_0^\infty \langle P_{ij}(t_0) P_{ij}(t_0 + t) \rangle dt \tag{2}$$

Although several expressions exist to fit dynamic properties for a fluid, we find that the VFT expression was the simplest to fit and use and we did not see any advantage using more complex functional forms [14]. The VFT function was used to fit the resulting self-diffusion and viscosity data (Equation 3). In the VFT expression, A, B, and T_0 are fitting constants. x is either self-diffusion or viscosity depending on which data was used for fitting.

$$log_{10}(x) = A + \frac{B}{T - T_0} \tag{3}$$

2.3 Characteristics Temperatures

Seven temperatures were calculated from MD: T_{gm} , T_g^* , T^* , T_A^* , T_g' , T', and T_A' . T_l was also considered but was taken from experimental data or the Alloy Phase Diagram Database from the American Society for Metals (ASM) International. Table B1 lists the system and the corresponding diagram used from ASM for T_l values. Here we describe how each characteristic temperature was determined. T_{gm} was calculated via methods used in Refs. [33, 34] which use a change in the potential energy, E_{pot} , slope between high and low temperature regimes to determine T_{qm} . The change of slope is typically acquired through a "knee" in a heat capacity curve with respect to temperature but we did not use this approach due to issues with numerical noise. We find the change in slope as follows. We perform a fit to E_{pot} vs. temperature using three piecewise linear fits, which represent the behavior of the system in the liquid, supercooled, and glassy phases. The three fitted lines are chosen to minimize the squared residuals using the package in Ref. [35]. An example of the fitting is shown in Figure 1. We then determine T_{qm} as the intersection of the two lower temperature lines (the glassy and supercooled liquid lines). We note that the intersection of the two higher temperature lines generally gives a dynamical slow down temperature, T_s , as defined in Ref. [34]. We were not able to determine a robust T_s for all systems and we did not use this value as a characteristic temperature in this study. We used this approach to determine T_{gm} for all 95 compositions studied. The uncertainty in our estimate of T_{gm} is found from the standard error of the mean (SEM) across the 2 cooling runs. The average SEM for T_{gm} across multiple compositions were 19 K, which is adequately low given the other uncertainties in this overall analysis.

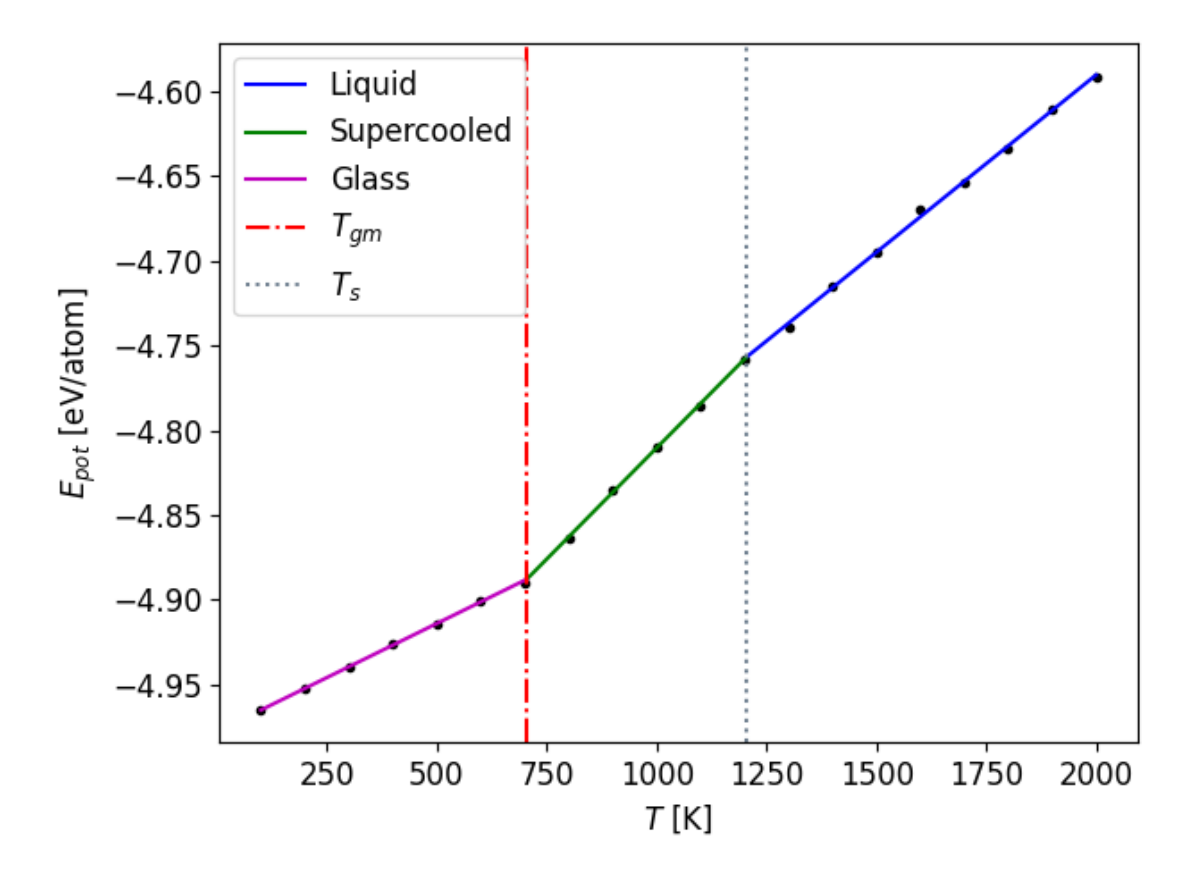


Figure 1: The results of a three part piecewise linear fit to the potential energy vs. temperature for $Cu_{50}Zr_{50}$. The transition from low-temperature glassy to mid-temperature supercooled liquid regimes is shown by the red vertical line which denotes the molecular dynamic glass transition temperature for a single run.

Self-diffusion and viscosity follow an Arrhenius behavior at high temperatures. At lower temperatures, cooperative motion becomes more significant leading to a deviation from Arrhenius behavior [6, 36]. A simple algorithm was applied to consistently compute T'_A and T^*_A across multiple compositions. First, self-diffusion and viscosity values were fit to VFT and a linear function. We then compared the two fits to see where they deviated and used that measure to determine the characteristic temperature. More specifically, we first started with all the data points. Then, if the mean absolute residuals (MAR) of the linear fit were more than the VFT fit by an amount greater than 0.005 for either self-diffusion or viscosity in their respective log_{10} units, the lowest temperature points were excluded from linear fits until the linear minus VFT MAR equaled or fell below the threshold. The computed T'_A and T^*_A denote the lowest temperatures where VFT and Arrhenius fits are approximately indistinguishable. The present approach provides a consistent definition for T'_A and T^*_A across the 95 studied compositions. The uncertainty in our estimate of these characteristic temperatures is found similarly to T_{gm} above from SEM across the 2 cooling runs. The algorithm used to compute T_A^{\prime} and T_A^* have average SEM values of 21 K and 11 K respectively for all compositions studied. More averaging could reduce uncertainties, but we find the uncertainties sufficient for the current work. A sample calculation of T_A^{\prime} and T_A^{*} are shown in Figures 2 and 3 respectively.

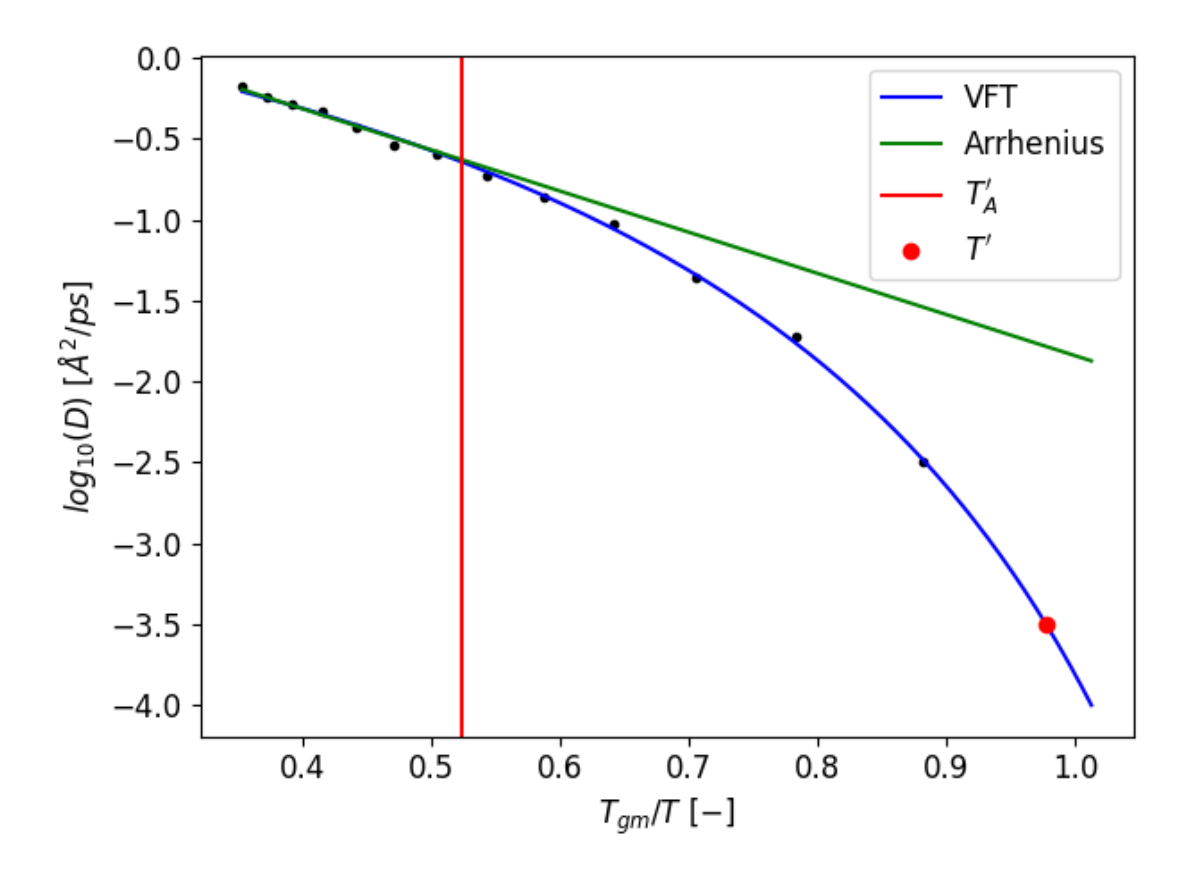


Figure 2: The self-diffusion behavior with respect to temperature for a single run of $Cu_{50}Zr_{50}$. The black points are the molecular dynamic self-diffusion for NVT isothermal holds. The blue and green curves are the VFT and high temperature Arrhenius fit to self-diffusion data respectively. The red point denotes the temperature at a user specified self-diffusion cutoff and the vertical line represent the temperature where self-diffusion deviates from Arrhenius behavior.

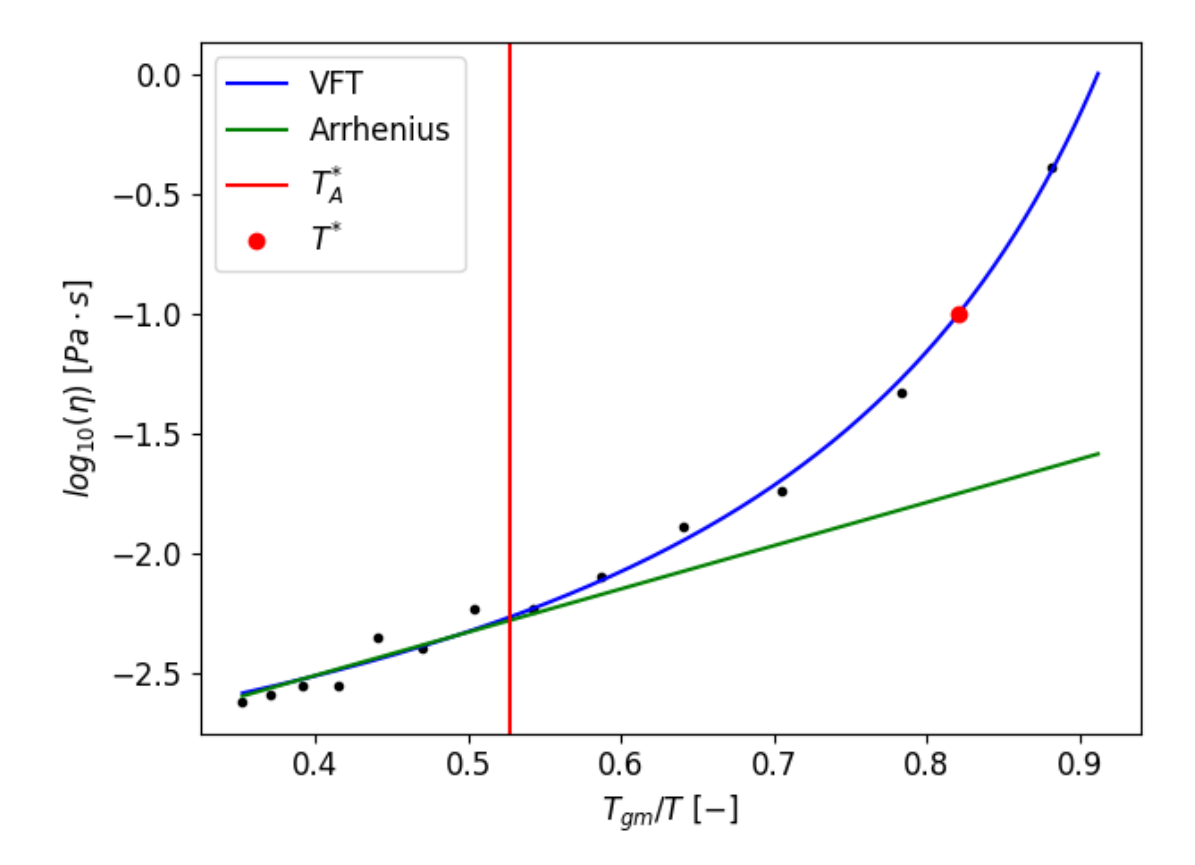


Figure 3: The viscosity behavior with respect to temperature for a single run of $Cu_{50}Zr_{50}$. The black points are the molecular dynamic viscosity for NVT isothermal holds. The blue and green curves are the VFT and high temperature Arrhenius fit to viscosity data respectively. The red point denotes the temperature at a user specified viscosity cutoff and the vertical line represent the temperature where viscosity deviates from Arrhenius behavior.

In a similar manner to T_A' and T_A^* calculation, T' and T^* were determined using fits to the VFT equation of self-diffusion and viscosity data respectively. T' was defined here as the temperature at which each composition reached a self-diffusion value of $10^{-3.5}$ Å/ps (Figure 2). Similarly, T^* was defined as the temperature where each composition reached a viscosity value of 10^{-1} $Pa \cdot s$ (Figure 3). The choice of cutoffs were as large as practical given a goal of being near data points acquired through MD to reduce extrapolation error from VFT. Using the same error methods for the characteristic temperatures described above gave average SEM for T' and T^* of 18 K and 9 K respectively. The values of T_g' and T_g^* were also determined from VFT fits to self-diffusion and viscosity. Again, using the same error methods, when the VFT functions were extrapolated to 10^{-12} Å $^2/ps$ and 10^{12} $Pa \cdot s$ for self-diffusion and viscosity, respectively, the average SEM for T_g' and T_g^* were 35 K and 31 K, respectively. Each CT along with its description can be seen in Table 1.

Table 1: The definitions for all CTs included in this study.

| CT | Description |
|--------------|---|
| T_{gm} | The glass transition temperature acquired from a potential |
| | energy versus temperature relationship. |
| T_g^* | The glass transition temperature acquired by extrapolating |
| | VFT viscosity to $10^{12} Pa \cdot s$. |
| T^* | The temperature where viscosity reaches $10^{-1} Pa \cdot s$. |
| T_A^* | The deviation from high temperature Arrhenius behavior in |
| | a viscosity versus temperature relationship. |
| T_q' | The glass transition temperature acquired by extrapolating |
| | VFT self-diffusion to $10^{-12} \text{ Å}^2/ps$. |
| T^{\prime} | The temperature where self-diffusion reaches $10^{-3.5} \text{ Å}/ps$. |
| T_A' | The deviation from high temperature Arrhenius behavior in |
| | a self-diffusion versus temperature relationship. |
| T_l | The liquidus temperature. |

2.4 Data

Experimental T_l , D_{max} , and melt-spun classification data were acquired through an online database with citations to papers included in the Data Availability section. Missing values of T_l were replaced by values read from ASM phase diagrams (see Table B1). Although T_l did not come from MD, previous studies show that MD calculation of T_l is possible, as discussed in the Introduction. When multiple D_{max} or T_l values were available for the same composition, the mean of the values were used. If any one of the melt-spun sheets resulted in fully or partially crystalline sheets, then that alloy was classified as a Poor GFA alloy. Fully amorphous sheets and alloys that had a D_{max} measure were classified as Good GFA alloys. As noted above, the data set containing only D_{max} data has 21 compositions, is a subset of the 95 total alloys, and is called the regression data set. The full set of 95 compositions is called the classification data and contains classes of Poor GFA (39 compositions = 41% of the data) and Good GFA (56 compositions = 59% of the data).

For our classification data, we can generate simple new features from products, ratios, summations, and differences (PRSDs) of the characteristic temperatures, which we call PRSD features. We can then compare the effect of the classification models using the PRSD features to models using our original set of characteristic temperatures as features. We are motivated to explore the PRSD features by the long history of studies using linear functions of PRSD features to predict different aspects of GFA, as discused in the Introduction. To construct the PRSD features, we follow the approach of Ref. [37]. We start with a set of characteristic temperatures defined as $A = \{T_{gm}, T_g^*, T^*, T_A^*, T_g', T', T_A', T_l\}$. From set A, summations and differences were taken between each of the features to construct set B. A sample feature contained in set B would be $(T_{gm}-T_l)$. Now define $C=A\cup B$. From C, we can take powers up to n for every element to produce set D. For instance, $(T_{qm}-T_l)^2$ is an element in set D. For our current work, we limited $n \in \{1,2\}$. Define set E as follows: $E = C \cup D$. For every element in E, we can take the inverse to produce set F. Continuing from our example, a possible element produced would be $1/(T_{am}-T_l)^2$. We then construct another set $G=E\cup F$. The final operation to generate features involves products between every combination of two elements from set G to produce set H. The final feature set was defined as $X = G \cup H$. This process produced a total of 32,896 features. As noted in the Results and Discussion section, PRSD features do not provide statistically significant improvements in learning GFA compared to using CTs alone. Hence, a larger space of features was not explored (e.g., $n \in \{1, 2, 3, 4, ...\}$ for power features). All data sets used for machine learning, models, and figures can be found at figshare and GitHub at Refs. [38] and [39] respectively.

2.5 Machine Learning

Scikit-learn was used for ML applications [40]. The XGBoost model type was attained from Ref. [41]. A standard scaler was used to transform all our features to have a mean of zero and a standard deviation of 1 for each dataset. When used in nested CV, the scaler is trained only on the training set and then used to transform both the training and test features.

Since the number of fitting points for our regression data are small, we fit a simple model to our characteristic temperatures of greatest importance. We use $log_{10}(D_{max})$ as the target feature. Raising D_{max} to a power within a logarithm like in Ref. [7] has no impact on the fitting $(log_{10}(D_{max}^x) = xlog_{10}(D_{max}))$ and ML models can account for the multiple by a real number xso no power is included. First, we trained a Least Absolute Shrinkage and Selection Operator (LASSO) model that minimized root mean squared error (RMSE) through a grid search of α hyperparameter values [42]. The α values considered were 10^{-5} to 10^{5} in a log_{10} grid of 100 values. The absolute value of weights from the fitted model denote the magnitude of the model's response with respect to a change in feature value which is a measure of the contribution each feature makes to predicting $log_{10}(D_{max})$. Using the two features with the highest weights, an OLS regression model was fit with an intercept term to produce the final model (using more features led to overfitting and reduced the CV accuracy, as might be expected given the complex physics and limited training data in the model). To assess the OLS model, 20 repeats of 3fold CV were performed to view the effects of prediction on data outside of the training set. Metrics reported for final regression models are the mean average error (MAE), coefficient of determination (R^2) , RMSE, and the $RMSE/\sigma$ where σ denotes the spread on predicted target values.

We implemented repeated nested CV to assess classification models. Model types included are Gradient Boosting (GB), eXtreme Gradient Boosting (XGBoost), and Random Forest (RF) which are ensemble models [41, 43, 44]. We used ensemble models because of their tendency to outperform linear models in D_{max} predictions in our past research [37]. Models were trained on PRSD feature and original characteristic temperature feature sets. Data were shuffled and split into 3 outer and 3 inner folds. The choice of hyperparameters that minimized RMSE were determined from the inner folds via a grid search (Table 2). The outer folds were used to assess a model's performance on data not used for training. Nested CV was performed 20 times which gave 60 test sets for each model and data set combination. Classification scores were averaged between all leave out sets. A two-sided T-test was performed between models trained on the original versus the PRSD feature sets to show if there was a statistically significant difference between training on the two feature sets.

Table 2: The grid of hyperparameters for XGBoost, GB, and RF models. The conventions of Scikit-learn and XGBoost were used for parameter names [40, 41].

| Model | Parameter | Values |
|---------|--------------------------|--------------------------|
| | $n_{estimators}$ | 30, 40, 50, 60, 100, 500 |
| RF | \max_{features} | sqrt, log2, None |
| | \max_{-depth} | 2, 3, 4, None |
| | learning_rate | 0.001, 0.01, 0.1, 0.2 |
| GB | $n_{-}estimators$ | 30, 40, 50, 60, 100, 500 |
| GD | \max_{features} | sqrt, log2, None |
| | \max_{-depth} | 2, 3, 4 |
| | learning_rate | 0.001, 0.01, 0.1, None |
| XGBoost | \max_{-depth} | 2, 3, 4, 5, None |
| AGDOOSt | subsample | 0.5, 0.8, 1.0, None |
| | gamma | 0, 1, 5, None |

All classification models were assessed with the area under the curve (AUC) from Precision-Recall (PR) curves and maximum F1 scores. F1 is defined as the harmonic mean between precision and recall. The baseline AUC for any PR curve is defined as P/(P+N) with P being the number of positive and N being the number of negative cases [45]. For the nested CV tests, PR curves where averaged together for the outer loops. The averaging was performed by first building a grid of horizontal values (recall for PR) from 0 to 1 with 1,000 linearly spaced values. Then data are linearly interpolated. This ensured that all averaged values were gridded equally for vertical averaging. For F1 scores, the maximum values were averaged between all outer folds.

SHapley Additive exPlanations (SHAP) provide feature interpretations by fairly allocating feature contributions via game theory, an approach developed by Professor Lloyd Shapley [46]. SHAP values were attained with the shap package in Ref. [47] and used to analyze feature contributions for an XGBoost model trained on all 95 cases (called the full-fit model) of our classification data set. We will show that the prediction contributions of the top 3 features agree with physical intuition of GFA.

3 Results and Discussion

First, we consider the regression data set and models. The OLS regression model fit from LASSO selected features was used to predict back onto the training set to produce the parity plot in Figure 4a. The $RMSE/\sigma$ was 0.48 which means that the RMSE of predicted $log_{10}(D_{max})$ values are well-below the spread in true values, σ . The characteristic temperatures with the highest absolute weights and therefore used in the model were T_l and T_A' . The sign of weights for T_l and T_A' were negative and positive respectively which follow expected theories. Assuming the experimental T_g is similar across studied compositions, a higher T_l represents a larger range of temperatures through which the supercooled liquid must remain stable without nucleating crystalline phases before producing a metallic glass. This argument is similar in spirit to that supporting T_{rg} as correlating with GFA, as proposed by Turnbull [1]. Conversely, a higher T_A' denotes a dynamic slowdown in a system at a higher temperature, which suppresses the ability of atoms to arrange themselves into an ordered structure and therefore suppresses crystallization and stabilizes glass formation. Higher T_l values should therefore reduce GFA while higher values of T_A' should increase GFA.

The closest model in literature to our OLS regression model was proposed in Ref. [7] as a linear combination of T_{rg} and m. Our model qualitatively agrees with the model in Ref. [7] in two ways. First, lower T_l for the OLS regression model generally results in higher T_{rg} and better GFA. Second, m denotes the viscosity of a system as it approaches experimental T_g . A larger m corresponds to less resistance to movement when cooling and vice versa which is similar to T_A' . Although the parameters across models are different, they both describe the degree of undercooling along with the mobility of atoms with respect to GFA. The model in Ref. [7] had an R^2 score of 0.980 while we had an R^2 score of 0.77. Our scores may have been worse due to the use of different variables, but perhaps also just because of the smaller number of compositions we could study along with our mixing of MD with approximate potentials and experimental data. Some of these aspects could be remedied in future work and potentially approach the outstanding accuracy of the model from Ref. [7] while still using MD derived features.

A more rigorous test of our OLS regression model was performed. The average of predicted values from leave-out compositions in 20 repeats of 3-fold CV along with their SEM is shown Figure 4b. As expected, the $RMSE/\sigma$ increased, with values changing from 0.48 to 0.68 ± 0.042 . The decrease in prediction performance can be explained by the generally complex dependence that might be expected for $log_{10}(D_{max})$ on the features, and in part by the lack of cases with low D_{max} values. The models fit only on high D_{max} cases will fail to predict the cases on the lower extreme. It is not surprising that fitting to few, unevenly distributed data results in a relatively inaccurate (Figure 4b) model, even when it may have first appeared promising during the full-fit without cross validation (Figure 4a).

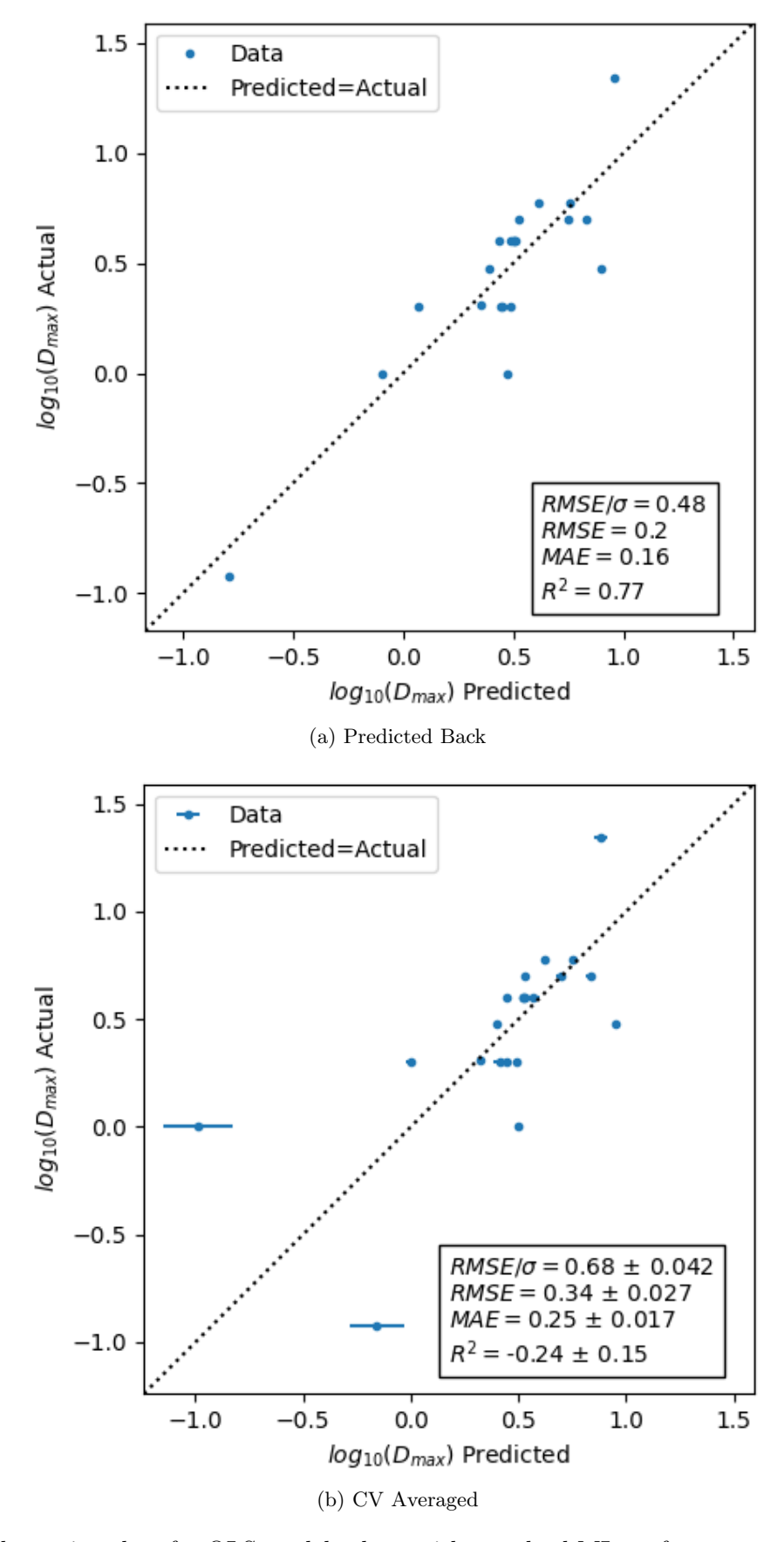


Figure 4: The parity plots for OLS models along with standard ML performance metrics. Each of the blue points denotes a prediction of D_{max} from a model. The black dotted line represents where ideal predictions would fall. We note a reduction in prediction ability of OLS models when a cross validation test was performed (predicted back compared to CV averaged).

Second, we consider the classification data set and models. Through nested CV with XGBoost, RF, and GB models fit on the original classification set and then the PRSD classification set, PR curves were produced as detailed in Sec. 2.5 and the scores were tabulated in Table 3. The use of XGBoost models yielded slightly better results than other models and is shown in Figure 5a. The AUC score for PR with Good GFA as positive was 0.84 ± 0.0097 with a baseline AUC of 0.59 ± 0.0086 . The average maximum F1 score was 0.82 ± 0.0067 . One way to understand the implications of the PR curve (Figure 5a) is that if one starts with a list of compositions similar to the training data, and one can accept finding just half the good GFA alloys in the list (50% recall), then one can be almost certain that the compositions one predicts as good GFAs are correctly identified (100% precision). As an example, consider searching a list of 100 compositions for GFA with 50 favorable glass formers. The XGBoost model might be expected to predict 25 of the alloys as good glass formers. Almost all 25 would likely be correct, but the model would find only 25 out of the 50 glass formers. A researcher could move along the PR curve to define an acceptable threshold to tune for the number of missed good glass formers while ensuring that a tolerable fraction of glasses studied will produce a glass.

Although the above results are encouraging, they are almost certainly optimistic when using the present model for predicting GFA of general alloys. First, one needs to consider the compositions in the data. Simulations were performed on only 17 chemical systems with a varying number of compositions in each system but 5-6 examples from each system on average. The outer folds used for model assessment therefore most likely contain compositions close to, although not exactly the same as, those used for model training. This will bias the CV scores to be much better than expected on data for totally new systems. Furthermore, new compositions outside the 17 studied here may be quite different in their underlying mechanisms, further reducing the applicability of the model. Finally, it should be noted that the present data is fairly well balanced, with about 59% of the data with good GFA. Even if the model accuracy is fairly well represented by the present PR on a new test data set, if the fraction of good GFA alloys is much lower, then the model will have much lower precision than found here. We therefore believe that the PR curve obtained here is exciting as it is evidence that GFA can be predicted from MD features based on characteristic temperatures, but it is not a robust guide for expected results on a general screening of alloys for GFA.

Table 3: The classification scores for all model types. The PRSD classification data contains generated features from the classification set as outlined in Sec. 2.5.

| Model | Feature Set | Metric | Score | SEM |
|---------|---------------------|-----------------------------------|-------|--------|
| GB | Classification | Precision Recall AUC for Good GFA | 0.82 | 0.0086 |
| GB | Classification | Max F1 for Good GFA | 0.80 | 0.0061 |
| RF | Classification | Precision Recall AUC for Good GFA | 0.84 | 0.0078 |
| RF | Classification | Max F1 for Good GFA | 0.81 | 0.0059 |
| XGBoost | Classification | Precision Recall AUC for Good GFA | 0.84 | 0.0097 |
| XGBoost | Classification | Max F1 for Good GFA | 0.82 | 0.0067 |
| GB | PRSD Classification | Precision Recall AUC for Good GFA | 0.84 | 0.0095 |
| GB | PRSD Classification | Max F1 for Good GFA | 0.82 | 0.0065 |
| RF | PRSD Classification | Precision Recall AUC for Good GFA | 0.86 | 0.0096 |
| RF | PRSD Classification | Max F1 for Good GFA | 0.83 | 0.0069 |
| XGBoost | PRSD Classification | Precision Recall AUC for Good GFA | 0.85 | 0.0094 |
| XGBoost | PRSD Classification | Max F1 for Good GFA | 0.82 | 0.0063 |

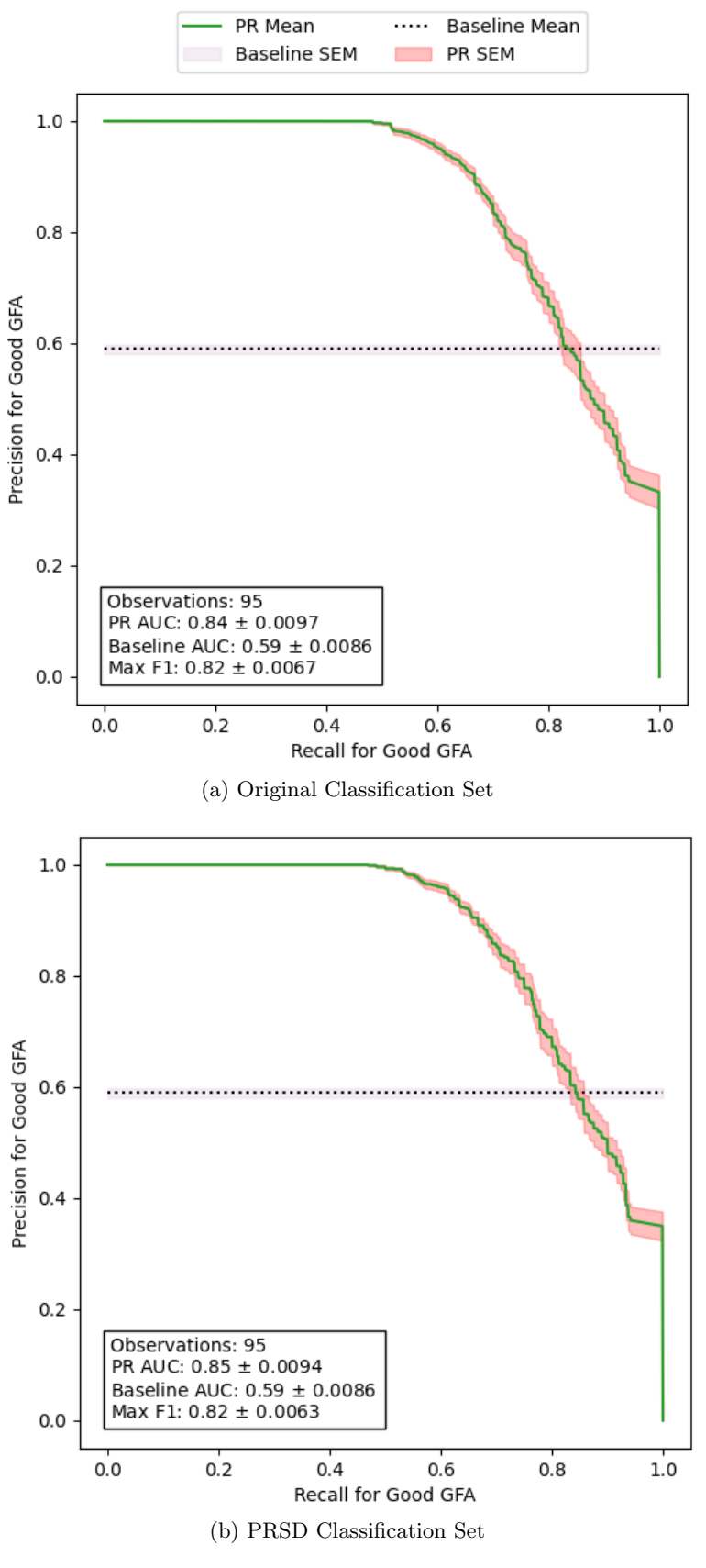


Figure 5: The comparison between XGBoost models trained on the original versus PRSD classification data sets. The green curve represents the precision and recall given a classification threshold averaged across outer fold test sets. The shaded red area is the SEM between averaged sets. The horizontal line is the average baseline from class counts from outer fold test sets along with the purple shaded region SEM.

The use of the PRSD features to fit models (Figure 5b) showed some improvement over the original classification feature set. Although initially promising, p-values computed from a two-sided T-test show that there was no statistically significant difference between learning from PRSD and original classification feature sets from 60 test observations. None of the p-values (Table 4) fell below 0.05 which is a commonly used cutoff for statistical significance. Because of the lesser complexity of the models fit with the original characteristic temperature feature set, the final evaluation metrics of XGBoost without PRSD features were reported.

Table 4: The p-values from two-sided T-tests.

| Model | Metric | P-Value |
|---------|-----------------------------------|---------|
| GB | Precision Recall AUC for Good GFA | 0.13 |
| GB | Max F1 for Good GFA | 0.22 |
| RF | Precision Recall AUC for Good GFA | 0.22 |
| RF | Max F1 for Good GFA | 0.21 |
| XGBoost | Precision Recall AUC for Good GFA | 0.59 |
| XGBoost | Max F1 for Good GFA | 0.51 |

The SHAP values for our full-fit XGBoost model are shown on Figure 6. The features that have the highest impact on the final prediction are at the top. Conversely, the bottom features have the lowest contribution on final predictions. Feature values to the right of the vertical line in Figure 6 push the final prediction to Good GFA while values to the left contribute to Poor GFA classification. The color of values denotes the scale of the feature values. The SHAP values are generally consistent with physical intuition, as can be seen by considering the trends of T^* , T_g^* , and T_l . The SHAP values show that higher values of T^* and T_g^* and lower values of T_l generally correlate with better GFA. Materials that have higher values of T^* experience higher viscosities at higher temperatures. These higher viscosities may slow down the kinetics of crystallization when cooling a molten alloy, supporting better GFA. However, lower values of T_l might decrease the range an alloy must cool through before vitrification in a time temperature transformation (TTT) diagram [12], also supporting better GFA. Similarly, higher values of T_g^* could narrow the amorphous cooling range on a TTT diagram, again supporting better GFA. These correlations between the SHAP values and these physically sound trends suggest that the model has captured some of the underlying physics behind GFA.

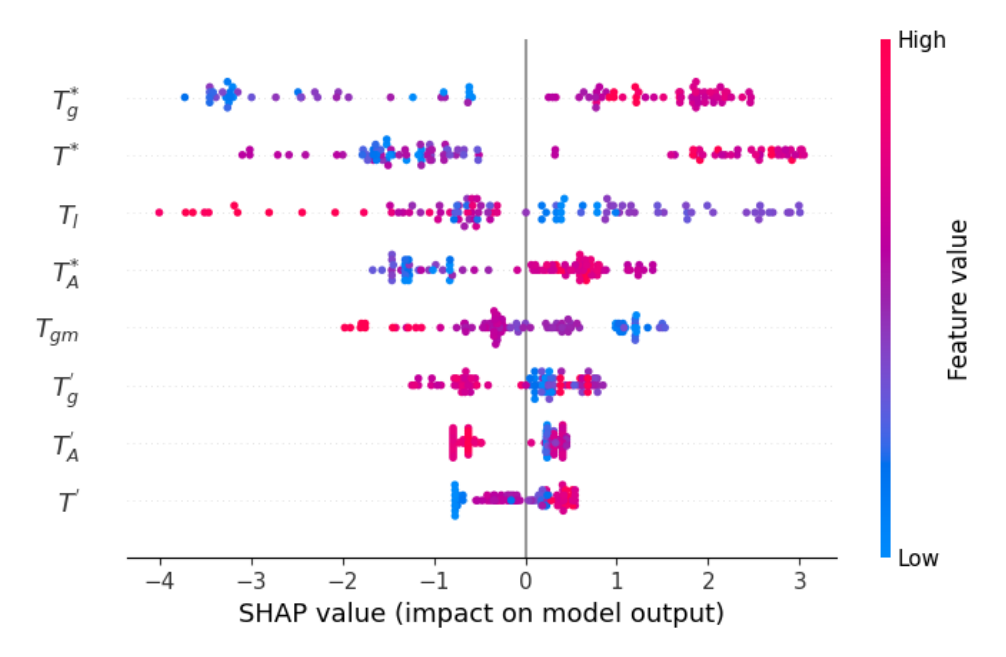


Figure 6: The SHAP values for our 8 characteristic temperatures for an XGBoost model. SHAP values from the figure denote the impact from each feature on the prediction of the model. Highest ranked features are displayed from the top to the bottom of the visual.

4 Summary and Conclusion

We used MD to calculate a set of characteristic temperatures for 95 metal alloys which were used to fit GFA for cases containing D_{max} and melt-spinning data. When using $log_{10}(D_{max})$ as our target, we find a 3-fold cross-validation RMSE score of 0.34 ± 0.027 for an OLS regression model, which was not significantly below the standard deviation of 0.43 for the 21 training cases. Only T_l and T'_A were used in the OLS model. Through nested CV, we assessed the capacity to learn poor from good glass formers for several models. XGBoost was slightly better than all other classification model types. Our average maximum F1 score for our RF classification predictions was 0.82 ± 0.0067 . Additionally, the AUC for classifying Good GFA on our PR curve was 0.84 ± 0.0097 which was greater than the baseline of 0.59 ± 0.0086 by 0.25. Our XGBoost models predict significantly higher than random guessing. We also determined that learning from PRSD features had no statistically significant effect for any classification tasks compared to learning on the characteristic temperatures themselves. Classification scores suggest that characteristic temperatures from MD can be used as features in machine learning models with predictive ability for GFA. This result provides a potential pathway to discovering new metallic glass alloys based on only simulations. However, to support such screening it is necessary to develop a larger training database that can train more quantitative models with larger ranges of chemistry in their domains of applicability.

Data Availability

The raw and processed data required to reproduce these findings are available to download from figshare at https://doi.org/10.6084/m9.figshare.14502135.v1 and GitHub at https://github.com/leschultz/Molecular-Dynamic-Characteristic-Temperatures-for-Predicting-Metallic-Glass-Forming-Ability.

Acknowledgements

Lane E. Schultz is grateful for the Bridge to the Doctorate: Wisconsin Louis Stokes Alliance for Minority Participation, National Science Foundation (NSF) award number HRD-1612530 as well as the University of Wisconsin– Madison Graduate Engineering Research Scholars (GERS) fellowship program for the financial support for graduate student investigation. Other authors gratefully acknowledge support from the NSF Designing Materials to Revolutionize and Engineer our Future (DMREF) program, Division of Materials Research (DMR), METAL & METALLIC NANOSTRUCTURES, award number #1728933. All simulation and machine learning were performed with the computational resources provided by the Extreme Science and Engineering Discovery Environment (XSEDE), National Science Foundation Grant No. OCI-1053575.

Appendix A

We explain in detail the viscosity calculations used in this work. Because practical MD has a finite run time, the integral form Equation 2 has an upper time limit of t_s . MD is also discrete so integration was represented with summation instead. Reformulation of Equation 2 yields the following:

$$\eta = \lim_{t_s \to \infty} \frac{V}{k_B T} \int_0^{t_s} \langle P_{ij}(t_0) P_{ij}(t_0 + t) \rangle_{t_0} dt \tag{A1}$$

$$\eta = \lim_{t_s \to \infty} \eta_{t_s} \tag{A2}$$

$$\eta_{t_s} = \frac{V}{k_B T} \int_0^{t_s} \left\langle P_{ij}(t_0) P_{ij}(t_0 + t) \right\rangle_{t_0} dt \tag{A3}$$

$$\eta_{t_s} = \frac{V}{k_B T} \lim_{\delta t \to 0} \sum_{t=0}^{t_s} \delta t \left\langle P_{ij}(t_0) P_{ij}(t_0 + t) \right\rangle_{t_0}$$
(A4)

In Equation A3, η_{t_s} is the approximate value of viscosity when the integral is only taken for a finite time t_s . The thermodynamic average $\langle \rangle_{t_0}$ of pressure values was performed by averaging over several time origins, t_0 , separated by a time lag. We take this average over different t_0 values, each separated by multiples of 0.1 ps, to obtain a value of η_{t_s} every 100 ps. Pressure values with equal time separations are then averaged and integrated 100 times to get the total η_{t_s} over the full 10 ns isothermal hold. To further explain, consider the following for autocorrelation of a quantity $P = P_{ij}$:

$$\langle P(t_0)P(t_0+t)\rangle = C_{PP}(t_0, t_0+t)$$
 (A5)

(because of time-translation invariance)

$$C_{PP}(t_0, t_0 + t) = C_{PP}(j\Delta t) \tag{A6}$$

(because of ergodicity)

$$C_{PP}(j\Delta t) = \frac{1}{N-j} \sum_{i=0}^{N-1-j} P(i\Delta t)P((i+j)\Delta t)$$
(A7)

where j is the separation between frames, Δt is the sample interval, and N is the total number of frames for a 100 ps period. See Refs. [48, 49] for further details. As an example, consider separations of $j \in \{0, 1, 2, N-1\}$ with $\Delta t = 100$ frames (equivalently 0.1 ps):

Average with zero lag at j = 0

$$C_{PP}(0) = \frac{1}{N} \sum_{i=0}^{N-1} P(100i)P(100i)$$

Average with 100 frame lag at j = 1

$$C_{PP}(100) = \frac{1}{N-1} \sum_{i=0}^{N-2} P(100i)P((i+1)100)$$

Average with 200 frame lag at j = 2

$$C_{PP}(200) = \frac{1}{N-2} \sum_{i=0}^{N-3} P(100i)P((i+2)100)$$

Average with maximum lag at j = N-1 $C_{PP}(100(N-1)) = P(0)P((N-1)100)$

Each time lag from $C_{PP}(j\Delta t)$ was averaged. For example, the very first step in MD produces one autocorrelation measure of P_{ij} with zero time lag. Then, the first 100 ps interval generates another 1000 values that are averaged with the previous for a mean value from 1001 observations with zero time lag. After 200 ps, there are a total of 2001 values with zero time lag to average. The same procedure was repeated for each possible time lag for the total 10 ns per isothermal hold. The integral with respect to each time lag average of the autocorrelation function of P_{ij} was used to compute viscosity with Equation A8 where $\tau = j\Delta t$.

$$\eta_{t_s} = \frac{V}{k_B T} \lim_{\delta \tau \to 0} \sum_{\tau=0}^{t_s} \delta \tau C_{PP}(\tau)$$
(A8)

To ensure a settled viscosity measurement, the final 2 ns were gathered from NVT simulations, the gradient of viscosity with respect to time was taken to acquire slopes, and then the mean of the slopes was taken. If the mean slope was below 10^{-5} Pa, then data were considered stable and therefore converged. For the converged cases, the average over the final 2 ns was used to determine our viscosity measurement. We average values because there are some minor viscosity fluctuations as seen in Figure A1.

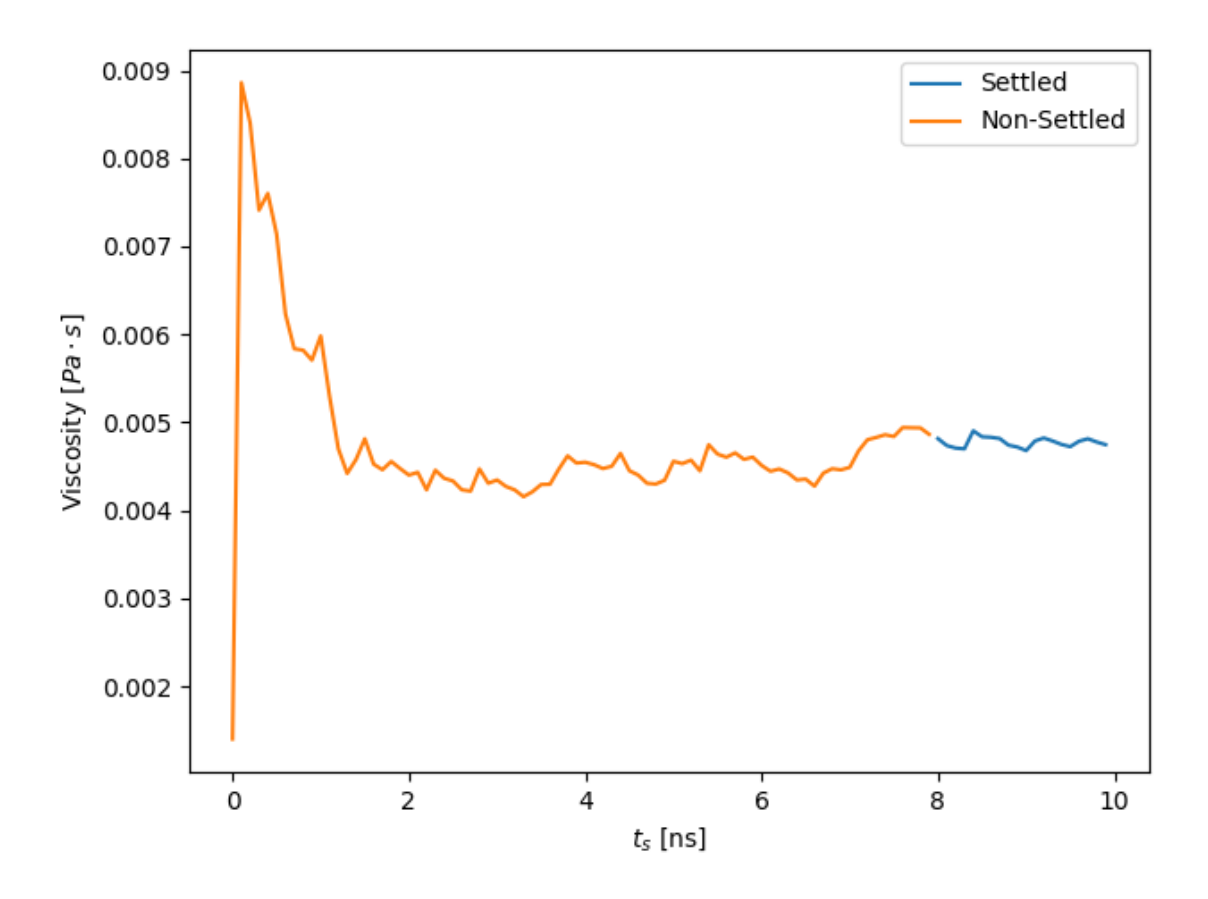


Figure A1: The running integral for viscosity of a single run of $Cu_{50}Zr_{50}$ at 1100 K. The curve is the pressure autocorrelation integrals taken every of 100 ps. The blue portion of the curve contains data used for convergence analysis of viscosity.

Appendix B

Table B1: The phase diagrams used from ASM International for \mathcal{T}_l values.

| System | Reference |
|--------|---|
| Ag-Cu | Silver-Copper Binary Phase Diagram (2007 Cao W.) |
| Al-La | Aluminum-Lanthanum Binary Phase Diagram (2000 Okamoto H.) |
| Al-Zr | Aluminum-Zirconium Binary Phase Diagram (2002 Okamoto H.) a |
| Al-Cu | Aluminum-Copper Binary Phase Diagram (1991 Chen S.) |
| Al-Ti | Aluminum-Titanium Binary Phase Diagram (2012 Wang H.) |
| Al-Ni | Aluminum-Nickel Binary Phase Diagram (2005 Miettinen J.) |
| Al-Sm | Aluminum-Samarium Binary Phase Diagram (2007 Delsante S.) |
| Al-Co | Aluminum-Cobalt Binary Phase Diagram (2004 Ohtani H.) |
| Cu-Zr | Copper-Zirconium Binary Phase Diagram (2010 Kang D.H.) a |
| Fe-Ni | Iron-Nickel Binary Phase Diagram (1991 Swartzendruber L.J.) d |
| Mg-Y | Magnesium-Yttrium Binary Phase Diagram (2008 Guo C.) |
| Nb-Ni | Niobium-Nickel Binary Phase Diagram (2007 Tokunaga T.) |
| Ni-Ti | Nickel-Titanium Binary Phase Diagram (2010 Agraval P.G.) |
| Ni-Zr | Nickel-Zirconium Binary Phase Diagram (2007 Wang N.) |
| Pd-Si | Palladium-Silicon Binary Phase Diagram (2006 Du Z.) b |

References

- [1] D. Turnbull, "Under What Conditions Can A Glass Be Formed?", Contemporary Physics, vol. 10, no. 5, pp. 473–488, Sep. 1969, ISSN: 13665812. DOI: 10.1080/00107516908204405. [Online]. Available: http://www.tandfonline.com/doi/abs/10.1080/00107516908204405.
- [2] Z. Long, H. Wei, Y. Ding, P. Zhang, G. Xie, and A. Inoue, "A new criterion for predicting the glass-forming ability of bulk metallic glasses", *Journal of Alloys and Compounds*, vol. 475, no. 1-2, pp. 207–219, 2009. DOI: 10.1016/j.jallcom.2008.07.087.
- [3] R. Deng, Z. Long, L. Peng, D. Kuang, and B. Ren, "A new mathematical expression for the relation between characteristic temperature and glass-forming ability of metallic glasses", Journal of Non-Crystalline Solids, vol. 533, no. January, p. 119829, 2020, ISSN: 00223093. DOI: 10.1016/j.jnoncrysol.2019.119829. [Online]. Available: https://doi.org/10.1016/j.jnoncrysol.2019.119829.
- [4] J. Xiong, T. Y. Zhang, and S. Q. Shi, "Machine learning prediction of elastic properties and glass-forming ability of bulk metallic glasses", MRS Communications, vol. 9, no. 2, pp. 576–585, 2019, ISSN: 21596867. DOI: 10.1557/mrc.2019.44.
- [5] R. Dai, R. Ashcraft, A. K. Gangopadhyay, and K. F. Kelton, "Predicting metallic glass formation from properties of the high temperature liquid", Journal of Non-Crystalline Solids, vol. 525, no. October, p. 119673, 2019, ISSN: 00223093. DOI: 10.1016/j.jnoncrysol. 2019.119673. [Online]. Available: https://doi.org/10.1016/j.jnoncrysol.2019. 119673.
- [6] A. Jaiswal, T. Egami, K. F. Kelton, K. S. Schweizer, and Y. Zhang, "Correlation between Fragility and the Arrhenius Crossover Phenomenon in Metallic, Molecular, and Network Liquids", 2016. DOI: 10.1103/PhysRevLett.117.205701. [Online]. Available: https://journals.aps.org/prl/pdf/10.1103/PhysRevLett.117.205701.
- [7] W. L. Johnson, J. H. Na, and M. D. Demetriou, "Quantifying the origin of metallic glass formation", *Nature Communications*, vol. 7, no. 1, p. 10313, Dec. 2016, ISSN: 20411723. DOI: 10.1038/ncomms10313. [Online]. Available: http://www.nature.com/articles/ncomms10313.
- [8] J. Hafner, "Theory of formation of metallic glasses. II", *Physical Review B*, vol. 28, no. 4, pp. 1734–1739, Aug. 1983, ISSN: 01631829. DOI: 10.1103/PhysRevB.28.1734. [Online]. Available: https://journals.aps.org/prb/abstract/10.1103/PhysRevB.28.1734.
- [9] Q. J. Hong and A. Van De Walle, "Prediction of the material with highest known melting point from ab initio molecular dynamics calculations", *Physical Review B Condensed Matter and Materials Physics*, vol. 92, no. 2, pp. 1–6, 2015, ISSN: 1550235X. DOI: 10.1103/PhysRevB.92.020104.
- [10] R. Jinnouchi, F. Karsai, and G. Kresse, "On-the-fly machine learning force field generation: Application to melting points", *Physical Review B*, vol. 100, no. 1, 2019, ISSN: 2469-9950. DOI: 10.1103/physrevb.100.014105. arXiv: 1904.12961.
- [11] L. C. R. Aliaga, L. V. Lima, G. M. Domingues, I. N. Bastos, and G. A. Evangelakis, "Experimental and molecular dynamics simulation study on the glass formation of Cu–Zr–Al alloys", *Materials Research Express*, vol. 6, no. 4, p. 045202, Jan. 2019, ISSN: 20531591. DOI: 10.1088/2053-1591/aaf97e. [Online]. Available: https://doi.org/10.1088/2053-1591/aaf97e.
- [12] J. D. Musgraves, J. Hu, and L. Calvez, Eds., Springer Handbook of Glass, 1st ed. West Henrietta, NY, USA: Springer International Publishing, 2019, pp. XXXVI, 1841, ISBN: 978-3-319-93728-1. DOI: 10.1007/978-3-319-93728-1.

- [13] D. V. Louzguine-Luzgin and A. I. Bazlov, "Crystallization of fcc and bcc liquid metals studied by molecular dynamics simulation", *Metals*, vol. 10, no. 11, pp. 1–11, 2020, ISSN: 20754701. DOI: 10.3390/met10111532.
- [14] M. E. Blodgett, T. Egami, Z. Nussinov, and K. F. Kelton, "Proposal for universality in the viscosity of metallic liquids", *Scientific Reports*, vol. 5, pp. 1–8, 2015, ISSN: 20452322. DOI: 10.1038/srep13837. arXiv: 1407.7558. [Online]. Available: http://dx.doi.org/ 10.1038/srep13837.
- [15] C. Chen, H. Zeng, Y. Deng, J. Yan, Y. Jiang, G. Chen, Q. Zu, and L. Sun, "A novel viscosity-temperature model of glass-forming liquids by modifying the eyring viscosity equation", *Applied Sciences (Switzerland)*, vol. 10, no. 2, 2020, ISSN: 20763417. DOI: 10. 3390/app10020428.
- [16] A. K. Gangopadhyay, C. E. Pueblo, R. Dai, M. L. Johnson, R. Ashcraft, D. Van Hoesen, M. Sellers, and K. F. Kelton, "Correlation of the fragility of metallic liquids with the high temperature structure, volume, and cohesive energy", *The Journal of Chemical Physics*, vol. 146, no. 15, p. 154 506, Apr. 2017, ISSN: 0021-9606. DOI: 10.1063/1.4981011. [Online]. Available: http://aip.scitation.org/doi/10.1063/1.4981011.
- [17] A. Gangopadhyay and K. Kelton, "Recent progress in understanding high temperature dynamical properties and fragility in metallic liquids, and their connection with atomic structure", Journal of Materials Research, vol. 32, no. 14, pp. 2638–2657, Jul. 2017, ISSN: 0884-2914. DOI: 10.1557/jmr.2017.253. [Online]. Available: https://www.cambridge.org/core/product/identifier/S0884291417002539/type/journal%7B%5C_%7Darticle.
- [18] R. Dai, A. Gangopadhyay, R. Chang, and K. Kelton, "A method to predict the glass transition temperature in metallic glasses from properties of the equilibrium liquid", *Acta Materialia*, vol. 172, pp. 1–5, Jun. 2019, ISSN: 1359-6454. DOI: 10.1016/J.ACTAMAT.2019. 04.034. [Online]. Available: https://www.sciencedirect.com/science/article/pii/S1359645419302368.
- [19] F. Puosi, N. Jakse, and A. Pasturel, "Dynamical, structural and chemical heterogeneities in a binary metallic glass-forming liquid", *Journal of Physics Condensed Matter*, vol. 30, no. 14, Mar. 2018, ISSN: 1361648X. DOI: 10.1088/1361-648X/aab110.
- [20] A. C. Angell, "Formation of Glasses from Liquids and Biopolymers", Science, vol. 267, no. 5206, pp. 1924–1935, 1995. DOI: 10.1126/science.267.5206.1924. [Online]. Available: papers2://publication/uuid/46ED95A9-CC48-4242-A7C5-9438976B8C42.
- [21] Y. Chen, W. Zhang, and L. Yu, "Hydrogen Bonding Slows Down Surface Diffusion of Molecular Glasses", Journal of Physical Chemistry B, vol. 120, no. 32, pp. 8007–8015, 2016, ISSN: 15205207. DOI: 10.1021/acs.jpcb.6b05658.
- [22] S. Plimpton, "Fast parallel algorithms for short-range molecular dynamics", Journal of Computational Physics, vol. 117, no. 1, pp. 1–19, Mar. 1995, ISSN: 00219991. DOI: 10.1006/jcph.1995.1039.
- [23] C. A. Becker, F. Tavazza, Z. T. Trautt, and R. A. Buarque De Macedo, "Considerations for choosing and using force fields and interatomic potentials in materials science and engineering", Current Opinion in Solid State and Materials Science, vol. 17, no. 6, pp. 277–283, 2013, ISSN: 13590286. DOI: 10.1016/j.cossms.2013.10.001. [Online]. Available: http://dx.doi.org/10.1016/j.cossms.2013.10.001.
- [24] Y. Q. Cheng, E. Ma, and H. W. Sheng, "Atomic level structure in multicomponent bulk metallic glass", *Physical Review Letters*, vol. 102, no. 24, pp. 1–4, 2009, ISSN: 00319007. DOI: 10.1103/PhysRevLett.102.245501.

- [25] Y. Q. Cheng, H. W. Sheng, and E. Ma, "Relationship between structure, dynamics, and mechanical properties in metallic glass-forming alloys", *Physical Review B Condensed Matter and Materials Physics*, vol. 78, no. 1, pp. 1–7, 2008, ISSN: 10980121. DOI: 10.1103/PhysRevB.78.014207.
- [26] T. Fujita, P. F. Guan, H. W. Sheng, A. Inoue, T. Sakurai, and M. W. Chen, "Coupling between chemical and dynamic heterogeneities in a multicomponent bulk metallic glass", *Physical Review B Condensed Matter and Materials Physics*, vol. 81, no. 14, pp. 1–4, 2010, ISSN: 10980121. DOI: 10.1103/PhysRevB.81.140204.
- [27] L. M. Hale, Z. T. Trautt, and C. A. Becker, "Evaluating variability with atomistic simulations: The effect of potential and calculation methodology on the modeling of lattice and elastic constants", *Modelling and Simulation in Materials Science and Engineering*, vol. 26, no. 5, 2018, ISSN: 1361651X. DOI: 10.1088/1361-651X/aabc05.
- [28] Q. J. Li, H. Sheng, and E. Ma, "Strengthening in multi-principal element alloys with local-chemical-order roughened dislocation pathways", *Nature Communications*, vol. 10, no. 1, pp. 1–11, 2019, ISSN: 20411723. DOI: 10.1038/s41467-019-11464-7. arXiv: 1904.07681. [Online]. Available: http://dx.doi.org/10.1038/s41467-019-11464-7.
- [29] H. W. Sheng, M. J. Kramer, A. Cadien, T. Fujita, and M. W. Chen, "Highly optimized embedded-atom-method potentials for fourteen FCC metals", *Physical Review B Condensed Matter and Materials Physics*, vol. 83, no. 13, pp. 1–20, 2011, ISSN: 10980121. DOI: 10.1103/PhysRevB.83.134118.
- [30] D. Rapaport, *The Art of Molecular Dynamics Simulation*. Cambridge University Press, 2007, ISBN: 9780521825689.
- [31] B. Hess, "Determining the shear viscosity of model liquids from molecular dynamics simulations", *Journal of Chemical Physics*, vol. 116, no. 1, pp. 209–217, 2002, ISSN: 00219606. DOI: 10.1063/1.1421362.
- [32] R. W. Zwanzig, "TIME-CORRELATION FUNCTIONS AND TRANSPORT COEFFI-CIENTS IN STATISTICAL MECHANICS National Bureau of Standards, Washington", Annu. Rev. Phys. Chem., vol. 16, pp. 67–102, 1964, ISSN: 0020-7136.
- [33] Y. Q. Cheng and E. Ma, "Indicators of internal structural states for metallic glasses: Local order, free volume, and configurational potential energy", *Applied Physics Letters*, vol. 93, no. 5, pp. 1–4, 2008, ISSN: 00036951. DOI: 10.1063/1.2966154.
- [34] H. W. Sheng, E. Ma, and M. J. Kramer, "Relating dynamic properties to atomic structure in metallic glasses", *Jom*, vol. 64, no. 7, pp. 856–881, 2012, ISSN: 10474838. DOI: 10.1007/s11837-012-0360-y.
- [35] C. F. Jekel and G. Venter, pwlf: a python library for fitting 1d continuous piecewise linear functions, 2019. [Online]. Available: https://github.com/cjekel/piecewise_linear_fit_py.
- [36] T. Iwashita, D. M. Nicholson, and T. Egami, "Elementary Excitations and Crossover Phenomenon in Liquids", 2013. DOI: 10.1103/PhysRevLett.110.205504. [Online]. Available: https://journals.aps.org/prl/pdf/10.1103/PhysRevLett.110.205504.
- [37] L. E. Schultz, B. Afflerbach, C. Francis, P. M. Voyles, I. Szlufarska, and D. Morgan, "Exploration of characteristic temperature contributions to metallic glass forming ability", Computational Materials Science, vol. 196, p. 110494, 2021, ISSN: 0927-0256. DOI: https://doi.org/10.1016/j.commatsci.2021.110494. [Online]. Available: https://www.sciencedirect.com/science/article/pii/S0927025621002196.

- [38] D. Morgan, L. Schultz, I. Szlufarska, and B. Afflerbach, Molecular dynamic characteristic temperatures for predicting metallic glass forming ability, Apr. 2021. DOI: 10.6084/m9.figshare.14502135.v1. [Online]. Available: https://figshare.com/articles/dataset/Molecular_Dynamic_Characteristic_Temperatures_for_Predicting_Metallic_Glass_Forming_Ability/14502135/1.
- [39] L. E. Schultz, Molecular-Dynamic-Characteristic-Temperatures-for-Predicting-Metallic-Glass-Forming-Ability, Apr. 2021. [Online]. Available: https://github.com/leschultz/Molecular-Dynamic-Characteristic-Temperatures-for-Predicting-Metallic-Glass-Forming-Ability.git.
- [40] F. Pedregosa, G. Varoquaux, A. Gramfort, V. Michel, B. Thirion, O. Grisel, M. Blondel, P. Prettenhofer, R. Weiss, V. Dubourg, J. Vanderplas, A. Passos, D. Cournapeau, M. Brucher, M. Perrot, and E. Duchesnay, "Scikit-learn: Machine learning in Python", Journal of Machine Learning Research, vol. 12, pp. 2825–2830, 2011.
- [41] T. Chen and C. Guestrin, "XGBoost: A scalable tree boosting system", in *Proceedings* of the 22nd ACM SIGKDD International Conference on Knowledge Discovery and Data Mining, ser. KDD '16, San Francisco, California, USA: ACM, 2016, pp. 785–794, ISBN: 978-1-4503-4232-2. DOI: 10.1145/2939672.2939785. [Online]. Available: http://doi.acm.org/10.1145/2939672.2939785.
- [42] R. Tibshirani, "Regression shrinkage and selection via the lasso", Journal of the Royal Statistical Society. Series B (Methodological), vol. 58, no. 1, pp. 267–288, 1996, ISSN: 00359246. [Online]. Available: http://www.jstor.org/stable/2346178.
- [43] Y. L. Pavlov, "Random forests", Random Forests, pp. 1–122, 2019. DOI: 10.1201/9780429469275-8.
- [44] J. H. Friedman, "Greedy function approximation: A gradient boosting machine", Annals of Statistics, vol. 29, no. 5, pp. 1189–1232, 2001, ISSN: 00905364. DOI: 10.1214/aos/ 1013203451.
- [45] T. Saito and M. Rehmsmeier, "The precision-recall plot is more informative than the ROC plot when evaluating binary classifiers on imbalanced datasets", *PLoS ONE*, vol. 10, no. 3, pp. 1–21, 2015, ISSN: 19326203. DOI: 10.1371/journal.pone.0118432.
- [46] E. Štrumbelj and I. Kononenko, "Explaining prediction models and individual predictions with feature contributions", *Knowledge and Information Systems*, vol. 41, no. 3, pp. 647–665, 2014, ISSN: 02193116. DOI: 10.1007/s10115-013-0679-x.
- [47] S. M. Lundberg and S.-I. Lee, "A unified approach to interpreting model predictions", in Advances in Neural Information Processing Systems 30, I. Guyon, U. V. Luxburg, S. Bengio, H. Wallach, R. Fergus, S. Vishwanathan, and R. Garnett, Eds., Curran Associates, Inc., 2017, pp. 4765–4774. [Online]. Available: http://papers.nips.cc/paper/7062-a-unified-approach-to-interpreting-model-predictions.pdf.
- [48] Definitions, properties, and examples of correlation functions, Chemistry LibreTexts, Dec. 2020. [Online]. Available: https://chem.libretexts.org/@go/page/107272.
- [49] Correlation functions, GROMACS, 2019. [Online]. Available: https://manual.gromacs.org/documentation/2019-rc1/reference-manual/analysis/correlation-function.html.